ROYAL SOCIETY
OF CHEMISTRY

PAPER

Check for updates

Imidazolium–POSS–anthracene hybridfluorophores for sensitive and selective detection of nitroaromatic compounds (NACs) and polycyclic aromatic hydrocarbon (PAH) derivatives

Chenchira Pherkkhuntod,[a] Supphachok Chanmungkalakul,[b] Vuthichai Ervithayasuporn,[a] Worawat Meevasana,[c] Jonggol Tantirungrotechai [ID][a] and Thanthapatra Bunchuay [ID] *[ad]

Driven by environmental concerns and associated health risks, the chemical sensing of nitroaromatic compounds (NACs) and polycyclic aromatic hydrocarbon derivatives (PAH derivatives) has gained critical importance for monitoring organic pollutants. In this study, we report the design and synthesis of dual-responsive fluorescent sensors based on an imidazolium-functionalized polyhedral oligomeric silses-quioxane (POSS) scaffold incorporating an anthracene fluorophore (POSS–Im–An·X, where X = Br, BF_4, PF_6). The cooperative functions between the inorganic POSS core and the imidazolium unit enhance both the binding affinity toward electron-deficient organic guests and the stability of the anthracene emission unit in aqueous media. Photophysical studies revealed strong fluorescence in mixed aqueous–organic media (up to 15% v/v water) and a preferential response toward picric acid (PA), 2,4-dinitrophenol (DNP), and electron-deficient PAH derivatives. ^{1}H NMR titration and density functional theory (DFT) calculations indicate that the binding mechanism is primarily governed by charge–dipole and π–π interactions, leading to fluorescence quenching upon guest binding through donor-photoinduced electron transfer (d-PET) processes. Furthermore, the counter anion significantly influences solid-state emission through ion-pairing and molecular packing effects. These findings position POSS–Im–An·X as a versatile and robust fluorescent sensor for the simultaneous detection of NACs and PAH derivatives, offering a promising platform for environmental monitoring and pollutant remediation.

Introduction

Rapid industrial growth has outpaced the ability to effectively manage waste and emissions from manufacturing processes, resulting in persistent and long-term environmental damage. In urban environments, incomplete combustion of hydrocarbons generates various polycyclic aromatic hydrocarbon derivatives (PAH derivatives), which can undergo nitration reactions with

atmospheric nitrogen dioxide to form nitroaromatic compounds (NACs).[1,2] In addition to atmospheric processes, NACs are extensively introduced into the environment through anthropogenic activities, including the manufacture and use of dyes, polymers, pesticides, and explosives.[3,4] The accumulation of PAH derivatives and NACs in environmental matrices poses serious threats to ecosystems and human health, thereby necessitating the development of efficient and reliable methods for their detection and monitoring.[5–7] Conventional analytical techniques for detection of PAH derivatives and NACs, such as high-performance liquid chromatography (HPLC), gas chromatography mass spectrometry (GC-MS), and ion mobility spectrometry (IMS), offer high accuracy and reliability.[8–10] However, these techniques are generally confined to laboratory environments due to high operational costs, complex sample preparation procedures, and the requirement for skilled personnel. Consequently, increasing attention has been directed toward fluorescence-based sensing platforms, which enable sensitive, low-cost, and rapid on-site detection.[5,11–16]

[a] *Department of Chemistry, Center of Excellence for Innovation in Chemistry (PERCH-CIC), Faculty of Science, Mahidol University, Bangkok, Thailand. E-mail: thanthapatra.bun@mahidol.ac.th*

[b] *Institute of Sustainability for Chemicals, Energy and Environment (ISCE2), Agency for Science, Technology and Research (A*STAR), 8 Biomedical Grove, #07-01 Neuros Building, Singapore, 138665, Republic of Singapore*

[c] *School of Physics, Suranaree University of Technology and Synchrotron Light Research Institute, Nakhon Ratchasima, 30000, Thailand*

[d] *Center of Sustainable Energy and Green Materials, Mahidol University, Salaya, Nakhon Pathom, Thailand*

This journal is © The Royal Society of Chemistry 2026

J. Mater. Chem. C, 2026, **14**, 5699–5711 | **5699**

Recent advances in fluorescence sensing of PAH derivatives and NACs have emphasized rational sensor designs that exploit donor–acceptor interactions between electron-rich fluorophores and electron-deficient analytes.[17–21] In particular, conjugated polymers, porous organic frameworks, and hybrid materials have demonstrated remarkable sensitivity toward nitroaromatic explosives such as picric acid and dinitrophenols.[22–26] Polyaromatic fluorophores, including anthracene and pyrene, are widely employed as optical reporters owing to their extended π-conjugation and strong fluorescence emission.[27–33] Nevertheless, their poor aqueous solubility and aggregation propensity significantly limit practical environmental applications.

Polyhedral oligomeric silsesquioxane (POSS) has emerged as a versatile inorganic–organic hybrid scaffold due to its rigid Si–O–Si cage structure, excellent thermal stability, and tunable organic periphery.[34,35] In recent years, POSS-based materials have been actively explored in membranes, polymer nanocomposites, photo-functional materials, and sensing platforms, highlighting their potential for advanced environmental applications.[36–38] Notably, the incorporation of ionic or bulky substituents onto the POSS framework has been shown to enhance solubility, suppress aggregation, and improve sensing performance.

Previously, our group reported water-soluble fluorescent sensors incorporating imidazolium-functionalized pyrene and anthracene units.[39,40] The large aromatic surfaces enabled effective donor–acceptor interactions with various NACs, including nitrophenols and picric acid, resulting in pronounced fluorescence quenching in aqueous media. However, aggregation of polyaromatic fluorophores often reduces quantum efficiency and sensing performance.[41] To mitigate this limitation, bulky and sterically hindered substituents have been employed to suppress aggregation and enhance fluorescence signal-to-noise ratios. For example, bis-silsesquioxane-functionalized pyrene systems exhibited strong blue emission and selective quenching toward PAH derivatives, with density functional theory (DFT) calculations attributing the quenching mechanism to π–donor–π–acceptor interactions.[42]

In parallel, pyrene-based metal–organic frameworks (MOFs) and conjugated microporous polymers (CMPs) have demonstrated high sensitivity and low detection limits for NACs and PAH

derivatives.[43] Despite these advances, the development of POSS-based fluorescent sensors capable of efficient operation in aqueous or mixed aqueous–organic environments remains challenging, particularly in terms of solubility, aggregation control, and dual detection capability.[44] In this study, we report the design and synthesis of an imidazolium-functionalized polyhedral oligomeric silsesquioxane (POSS) bearing an anthracene fluorophore as a bifunctional fluorescence sensor for the simultaneous detection of NACs and PAH derivatives in aqueous–organic media. The sensor architecture was efficiently constructed via a one-step nucleophilic substitution reaction. Structurally, the sensor integrates three synergistic components: (i) an anthracene moiety that serves as an electron-rich fluorophore with strong and well-defined emission characteristics; (ii) an imidazolium spacer that enhances aqueous compatibility while modulating the electronic properties of the π–conjugated system; and (iii) a POSS core that provides exceptional thermal stability and broad solvent compatibility, facilitating potential integration into functional coatings and sensing platforms (Fig. 1).[45,46]

The photophysical properties of the sensor were systematically investigated across a range of solvent systems, revealing that a 15% (v/v) water/DMSO mixture offers optimal conditions for both qualitative and quantitative detection of NACs and PAH derivatives via UV-visible absorption and fluorescence spectroscopies. Notably, the sensor exhibited high sensitivity toward picric acid (PA), 2,4-dinitrophenol (DNP), and electron-deficient PAH derivatives. Mechanistic insights derived from NMR spectroscopy and computational modelling suggest that charge–dipole interactions, hydrogen bonding interactions, and π–π interactions collectively govern the sensor–analyte recognition process. This work advances the development of dual-function fluorescence sensors and provides a robust POSS-based platform for environmental detection of aromatic pollutants in complex aqueous matrices, with significant implications for ecological monitoring and pollutant remediation.

Experimental section

Materials and characterization

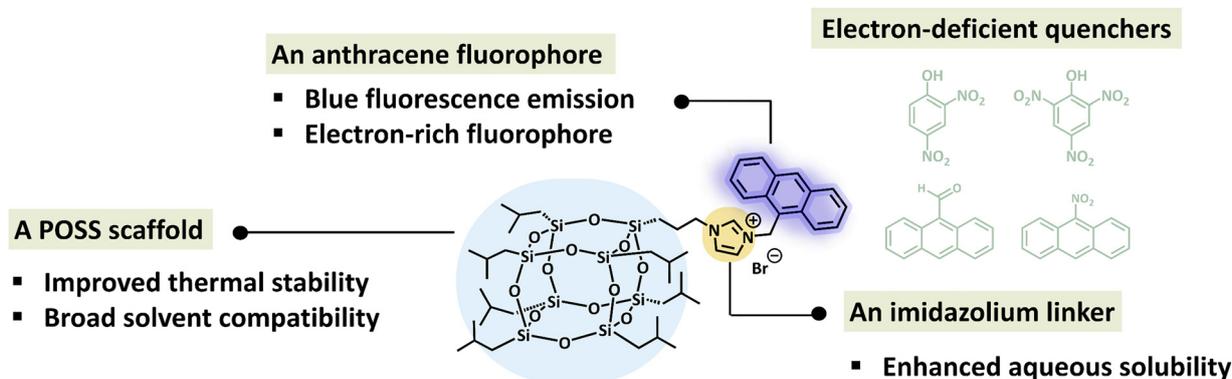The materials and experimental methods are described in the SI.

Fig. 1 An imidazolium-functionalized polyhedral oligomeric silsesquioxane (POSS) bearing an anthracene fluorophore.

Synthesis

Isobutyl–POSS–propyl-3-imidazole (POSS–Im). POSS–Im was synthesized following the modified procedure from the previously reported synthetic procedure.[47] Imidazole (2.3 g, 30 mmol) and POSS–Cl (1.5 g, 1.68 mmol) were added to a thick-walled tube, and then toluene (5 mL) was added. Subsequently, the mixture was stirred at 110 °C for 24 h. After that, the solution was evaporated to remove toluene *in vacuo*. The resulting crude product was extracted with diethyl ether and washed with DI water. The organic phase was evaporated to obtain a white solid powder (1.18 g, 65% yield). ^{1}H-NMR (400 MHz, CDCl$_3$): δ 7.87 (s, 1H), 7.15 (s, 1H), 6.94 (s, 1H), 4.02–3.98 (t, 2H), 1.88–1.80 (m, 9H), 0.96 (s, 21H), 0.94 (s, 21H), 0.61–0.59 (d, 16H); ^{13}C-NMR (100 MHz, CDCl$_3$): δ 137.1, 129.4, 118.8, 49.4, 25.8, 24.9, 24.0, 22.6, 9.2; ^{29}Si-NMR (79 MHz, CDCl$_3$): δ −67.6, −67.8, −67.9, −68.3; HRMS (ESI): Anal. calcd for $[C_{32}H_{72}N_2O_{12}Si_{18} + H]^+$ m/z = 925.3312, found m/z = 925.3339.

9-(Anthracenyl methyl)imidazolium bromide silsesquioxane cage (POSS–Im–An·Br). POSS–Im (0.3 g, 0.32 mmol) and Br-An (0.14 g, 0.48 mmol) were added into a thick-walled tube, and then DMF was added in this tube. Then the mixed solution was stirred at 110 °C for 1 day. This reaction evaporated the solvent. Then the residue product was decanted with diethyl ether until the solution color changed from yellow to clear to obtain a pale-yellow solid. The resulting product was dissolved with ethanol and carbon powder, and then this solution was filtered through Celite using a Büchner funnel. Then, the solvent was evaporated to obtain the final product (0.31 g, 86% yield). ^{1}H-NMR (400 MHz, CDCl$_3$): δ 10.90 (s, 1H), 8.60 (s, 1H), 8.38–8.36 (d, 2H), 8.08–8.06 (d, 2H), 7.69–7.65 (t, 2H), 7.55–7.52 (t, 2H), 6.90 (s, 1H), 6.76 (s, 1H), 6.67 (s, 2H), 4.32–4.28 (t, 2H), 1.96–1.93 (m, 2H), 1.83–1.79 (m, 7H), 0.94–0.93 (d, 21H), 0.91–0.89 (d, 21H), 0.59–0.56 (m, 16H); ^{13}C-NMR (100 MHz, CDCl$_3$): δ 137.4, 131.3, 131.0, 130.7, 129.6, 128.5, 125.7, 122.8, 121.7, 121.4, 120.6, 52.1, 46.0, 25.6, 24.0, 23.8, 22.4, 8.9; ^{29}Si-NMR (79 MHz, CDCl$_3$): δ −67.5, −67.8, −69.2; HRMS (ESI): Anal. calcd for $[C_{49}H_{83}N_2O_{12}Si_8 + H]^+$ m/z = 1116.4173, found m/z = 1115.4159.

Results and discussion

Synthesis and characterization

Initially, a mono-chloro functionalized POSS (POSS–Cl) was synthesized following a previously reported synthetic protocol.[48] A solution of POSS–OH precursor in dried THF was slowly reacted with 3-chloropropyltrichlorosilane at 0 °C overnight. The obtained crude product was further purified through recrystallization from a mixture of THF and MeOH, affording POSS–Cl in 64% yield with high purity as determined by ^{1}H-NMR analysis. A nucleophilic substitution reaction of POSS–Cl with imidazole in toluene at 110 °C afforded POSS–Im in a 65% yield. The reaction between POSS–Im and Br–An in DMF at 110 °C gave a 9-(anthracenyl methyl)imidazolium bromide silsesquioxane cage (POSS–Im–An·Br) in an 86% yield (Scheme 1). Finally, POSS–Im–An·Br was anion exchanged to
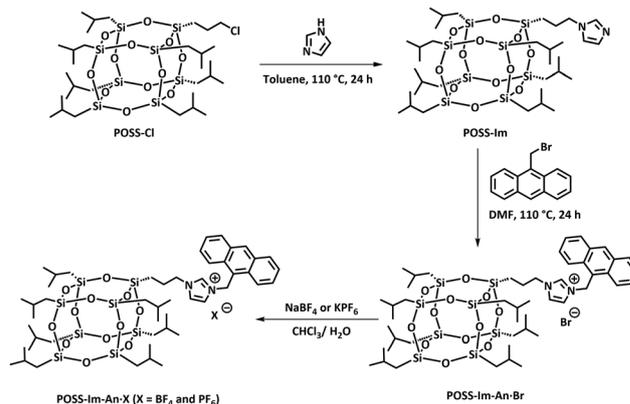
Scheme 1 Synthetic route for the preparation of POSS–Im–An·Br, followed by anion-exchange reactions to afford POSS–Im–An·BF$_4$ and POSS–Im–An·PF$_6$.

POSS–Im–An·BF$_4$ and POSS–Im–An·PF$_6$ by stirring a solution of POSS–Im–An·Br that was layered with a saturated solution of NaBF$_4$ and KPF$_6$, respectively.

All synthesized compounds were initially characterized by ^{1}H, ^{13}C, and ^{29}Si-NMR spectroscopy (Fig. S1–S14). A successful synthesis of POSS–Cl, POSS–Im, and POSS–Im–An·Br could be simply observed by monitoring the chemical shift of the terminal methylene protons (H$_a$) in all compounds. The H$_a$ signals are observed at the chemical shift of 3.52 in POSS–Cl, 4.00 in POSS–Im, and 4.30 in POSS–Im–An·Br, suggesting that incorporation of both imidazole and imidazolium functional groups into the POSS scaffold induced downfield perturbations of H$_a$ as a result of their electron-withdrawing properties. Moreover, POSS–Im showed characteristics of imidazole signals at the chemical shifts of 7.87 (H$_b$), 7.15 (H$_c$), and 6.94 (H$_d$) ppm. These signals were further shifted to 10.90 (H$_b$), 6.90 (H$_c$), and 6.76 (H$_d$) ppm in the ^{1}H-NMR spectrum of POSS–Im–An·Br concomitantly with emerging of signals attributed to anthracene moieties (H$_e$) at chemical shifts of 6.67 ppm (Fig. 2a–c and Fig. S3, S6, S9).

The ^{13}C-NMR spectra revealed a chemical shift of the C$_a$ signal at 47.4 ppm for POSS–Cl, which further downfield shifted to 49.4 ppm for POSS–Im. In addition, ^{13}C signals from the imidazole ring in POSS–Im emerged at chemical shifts of 137.2, 129.4, and 118.8 ppm. Incorporating the anthracene moiety into POSS–Im–An·Br shifted the C$_a$ signal to 52.1 ppm, with carbon signals from the anthracenyl group (C$_e$) at 45.9 ppm and the imidazolium moiety (C$_b$, C$_c$, and C$_d$) at 137.4, 121.7, and 121.4 ppm (Fig. S4, S7 and S10). The structure of POSS–Im–An·Br was further verified through ^{29}Si-NMR spectroscopy. The chemical shifts of ^{29}Si signals derived from the POSS core structure were observed at −67.6, −67.8, −67.9, and −68.3 ppm for POSS–Im, while ^{29}Si signals of POSS–Im–An·Br were observed at −67.5, −67.8, and −69.2 ppm (Fig. S8 and S11).

Thermogravimetric analysis (TGA) of all samples demonstrated improved thermal stability, as evidenced by the decomposition temperatures under air. The composition temperatures for POSS–Cl, POSS–Im, and POSS–Im–An·Br were

observed at 242 °C, 302 °C, and 305 °C, respectively. The main weight loss percentages for POSS–Cl, POSS–Im, and POSS–Im–An·Br were 61%, 66%, and 95%, respectively, correlating with the size of the substituents (Cl > Im > An) (Fig. S15–S17). In the case of POSS–Im–An·Br, the improved thermal stability is indicated by the initial weight loss occurring at 292 °C, which is higher than that of POSS–Cl. This suggests that the anthracene-imidazolium moiety significantly influences the thermal properties of the modified POSS, proving enhanced thermal stability because of bulky or aromatic substituents.[49–51]

POSS–Cl, POSS–Im, and POSS–Im–An·Br exhibit distinct PXRD patterns (Fig. S18), demonstrating that modifications to the substituents influence their crystal structures. The introduction of bulky and highly conjugated substituents, such as imidazole and anthracene, can significantly disrupt molecular packing.

A series of mono-anthracenyl functionalized imidazolium POSS compounds with different counter anions (POSS–Im–An·X, where X = Br, BF$_4$, and PF$_6$) were prepared (see SI), and fully characterized *via* ^{1}H-NMR, ^{13}C-NMR, ^{19}F-NMR spectroscopy, HRMS, and PXRD (Fig. S9–S21). Truncated ^{1}H-NMR spectra of POSS–Im–An·Br, POSS–Im–An·BF$_4$, and POSS–Im–An·PF$_6$ in CDCl$_3$ revealed the positions of the acidic proton of the imidazolium group (H$_b$) in each compound located at 10.90, 8.97, and 9.27 ppm, respectively (Fig. 2c–e and Fig. S12–S14). The result indicated that H$_b$ interacted with these anions through charge-assisted hydrogen bonding interactions in a low-polarity solvent such as CDCl$_3$. The high charge density and

coordinating anions, such as Br$^-$, formed strong hydrogen bonding with the imidazolium group and induced a significant downfield perturbation of H$_b$ compared to the chemical shift of these protons in POSS–Im–An·BF$_4$ and POSS–Im–An·PF$_6$.

These stark contrasts in H$_b$ chemical shifts were diminished when the spectra of the samples were recorded in a high polarity solvent such as d$_6$-DMSO (Fig. 3a).[52] ^{19}F-NMR spectra of POSS–Im–An·BF$_4$ and POSS–Im–An·PF$_6$ were recorded, and their ^{19}F signals were compared with those of two reference organic fluoride salts, TBABF$_4$ and TBAPF$_6$. ^{19}F signals of POSS–Im–An·PF$_6$ appeared at −71.6 and −73.5 ppm and those of POSS–Im–An·BF$_4$ appeared at −151.8 and −151.9 ppm, in contrast to the ^{19}F signals of the reference TBAPF$_6$ (−71.8 and −73.6 ppm) and TBABF$_4$ (−152.1 and −152.2 ppm) (Fig. 3b and c).

The similarity in PXRD patterns indicates that the primary crystal structures of POSS–Im–An·Br, POSS–Im–An·BF$_4$, and POSS–Im–An·PF$_6$ remain largely unchanged despite containing different counter ions (Fig. S19). This implies that the dominant intermolecular interactions responsible for crystal packing are likely occurring between the main molecular structures, rather than being mediated by the counterions.[53]

Photophysical properties

UV-visible and fluorescence spectroscopic measurements were carried out to investigate the photophysical properties of POSS–Im–An·Br at a fixed concentration in a range of polar protic and aprotic organic solvents, including MeOH, EtOH, DMSO, DMF, MeCN, and THF (Fig. S22 and Table S1). UV-visible absorption
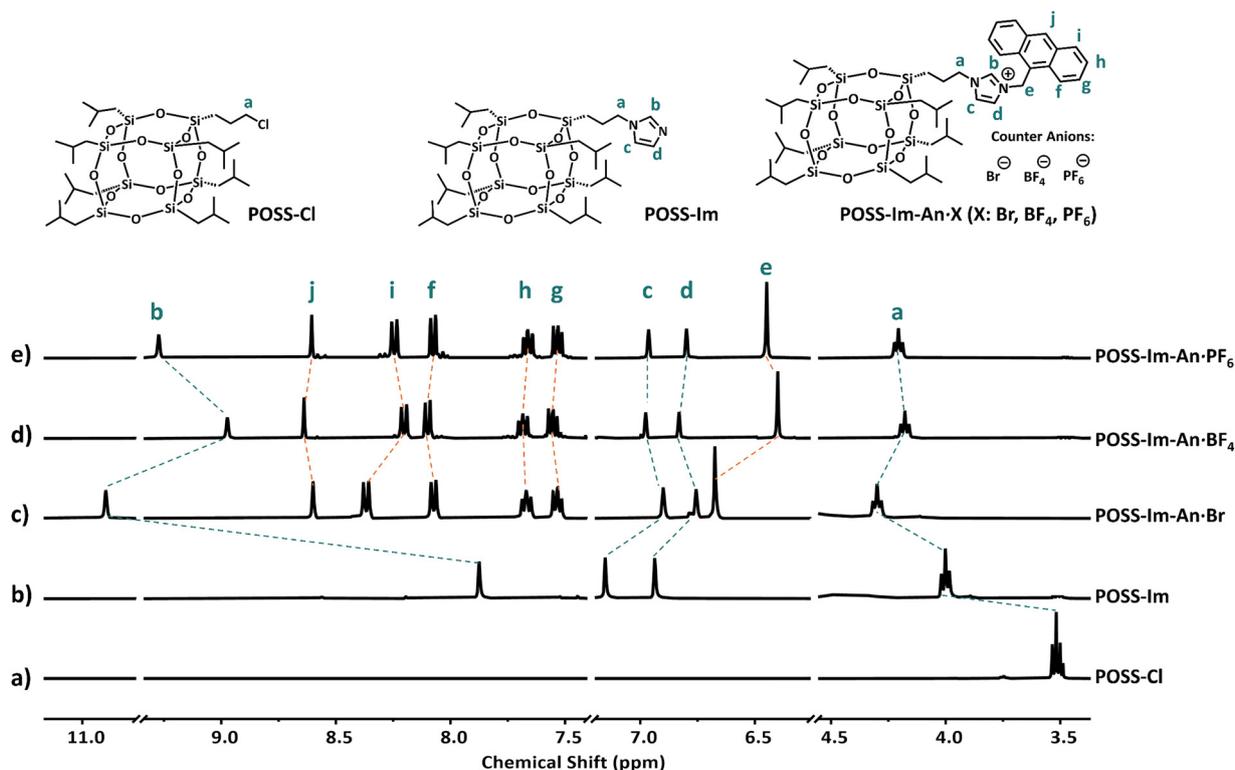

Fig. 2 Stacking of truncated ^{1}H-NMR spectra of (a) POSS–Cl, (b) POSS–Im, (c) POSS–Im–An·Br, (d) POSS–Im–An·BF$_4$ and (e) POSS–Im–An·PF$_6$ (CDCl$_3$, 400 MHz).

5702 | *J. Mater. Chem. C*, 2026, **14**, 5699–5711

This journal is © The Royal Society of Chemistry 2026
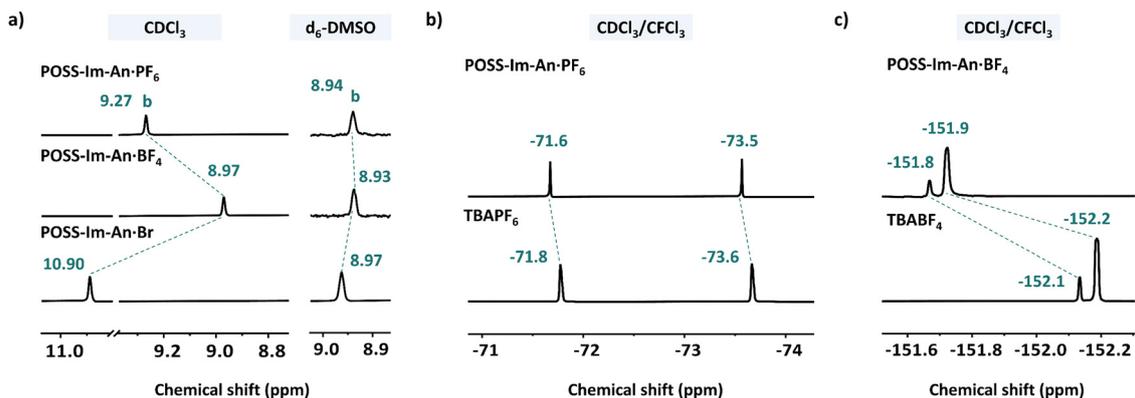
Fig. 3 (a) ^{1}H-NMR spectra of POSS–Im–An·X (X = Br, BF$_4$, and PF$_6$) recorded in CDCl$_3$ and d$_6$-DMSO, (b) ^{19}F-NMR spectra of POSS–Im–An·PF$_6$ and TBAPF$_6$, and (c) POSS–Im–An·BF$_4$ and TBABF$_4$ recorded in CDCl$_3$/CFCl$_3$.

spectra of POSS–Im–An·Br show three distinct absorption bands, centered approximately at 353, 371, and 391 nm, which are similar in all solvents. These bands indicate the characteristic π–π* transitions of the anthracene group (Fig. 4a).[54–56] In addition, the spectrum in water was also collected and showed significantly low absorption intensity, due to the self-aggregation and low solubility. Fluorescence emission spectra of POSS–Im–An·Br in different solvents revealed distinct emission spectra, centered approximately at 396, 419, and 440 nm, with the following order of emission intensity: DMSO > MeOH > DMF > EtOH > MeCN > THF > DI water (Fig. 4b). DMSO gave the most pronounced color and the

highest fluorescence intensity among the solvents examined when exposed to UV light. As a result, DMSO was chosen as the most suitable solvent for this investigation. In addition, the fluorescence emission signals were progressively quenched as the water content increased from 0% to 40% (v/v) and were completely quenched in the solution containing water up to 50% (v/v) (Fig. 4c–e). In solvent media with high water contents, POSS–Im–An·Br tends to aggregate and form a colloidal state. The hydrophobic nature of the aromatic anthracenyl moiety and isobutyl groups connected to the POSS scaffold results in aggregation in high water content media. The π–π interactions between anthracenyl aromatic units in POSS–Im–An·Br led to
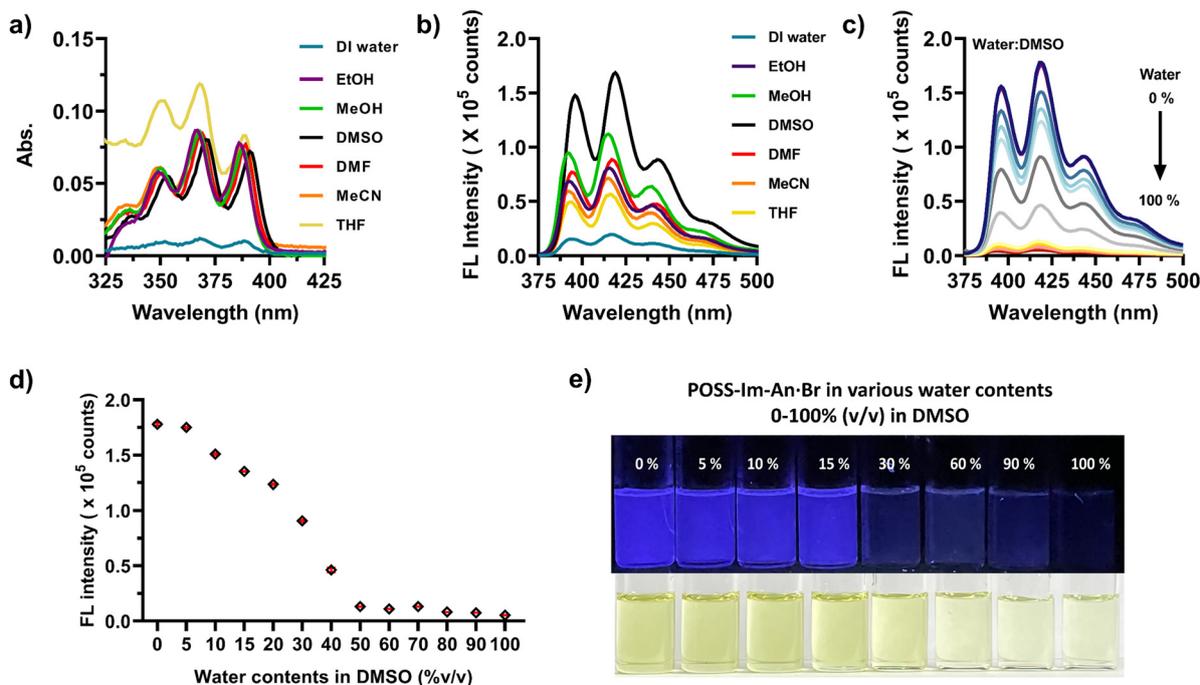

Fig. 4 (a) UV-visible absorption spectra and (b) fluorescence emission spectra of POSS–Im–An·Br solutions (1×10^{-6} M) in various solvents, (c) fluorescence emission spectra of POSS–Im–An·Br solutions (1×10^{-6} M) in DMSO containing varying amounts of water contents, (d) a plot representing the fluorescence emission intensity at 419 nm as a function of water content (%v/v) in DMSO, and (e) photograph illustrating changes in fluorescence emission in DMSO–water mixtures as the water content increases, viewed under UV light at 365 nm (upper) and room light (lower).

This journal is © The Royal Society of Chemistry 2026

J. Mater. Chem. C, 2026, **14**, 5699–5711 | **5703**

non-radiative decay pathways that suppress fluorescence signals.[57,58]

Solid-state and solution-state emission

A solution of POSS–Im–An·Br in 15% (v/v) water in DMSO displayed well-defined characteristic absorption bands of the anthracene moiety, with maxima at 353, 371, and 391 nm. Upon excitation under UV light, the solution produced sharp fluorescence peaks centered at 396, 419, and 440 nm (Fig. 5a). In contrast, the solid-state sample of POSS–Im–An·Br exhibited only a broad absorption band centered at 372 nm and a broad emission signal at 450 nm (Fig. 5b). The spectral broadening in the solid state indicates excimer formation and energy state distribution, a phenomenon where two anthracene moieties interact in an excited state through π–π interactions.[59] In solution, such interactions are minimal due to molecular motion and solvation effects that attenuate the degree of π–π interactions among anthracenyl units.[60]

Effect of counter anions

Solid samples of POSS–Im–An·Br, POSS–Im–An·BF$_4$, and POSS–Im–An·PF$_6$ are yellow powders that emit light in various colors, from green to strong yellow, when exposed to UV radiation, suggesting the influence of anions in solid-state emission (Fig. 6). This variation in emission behavior can be attributed to differences in electrostatic interactions between the [POSS–Im–An]$^+$ cation and its corresponding counter anion.[61–63] Smaller anions, such as Br$^-$, interact more strongly with cations, resulting in tighter ion-pair formation and more organized molecular packing in the solid state. Larger and weakly coordinating anions, such as PF$_6^-$ and BF$_4^-$, exhibited reduced electrostatic interactions with the cation, potentially leading to enhanced π–π interactions between chromophores.[64] These findings highlight the importance of counter-anion identity in tuning the photophysical properties of fluorophores in the solid state through combined electrostatic effects and packing-induced interactions (Fig. S23).[65,66]

Quantitative fluorescence titration studies

In this study, a series of NACs and PAH derivatives chosen were summarized and named using acronyms for clarity (Fig. 7).[9,67]

Quantitative fluorescence titration experiments of POSS–Im–An·Br with all selected NACs and PAH derivatives were performed in a 15% (v/v) water/DMSO aqueous solution to determine parameters including the Stern–Volmer constant (K_{sv}), binding affinity (K_a), limits of detection (LOD), and limits of quantification (LOQ) (Fig. S24).[68]

In the presence of NACs, POSS–Im–An·Br displayed different degrees of fluorescence quenching varying with the type of NAC. Upon addition up to 50 equivalents (equiv.) of NACs, POSS–Im–An·Br demonstrated considerable quenching of fluorescence signals only in the presence of PA and DNP, with 89% and 55% quenching, respectively, while other NACs failed to yield the same results (Table 1 and Fig. 8a). Linear Stern–Volmer plots determined the K_{sv} values for PA and DNP of 2.89×10^5 M^{-1} and 2.29×10^4 M^{-1}, respectively (Fig. 8d and Fig. S25). In addition, the Benesi–Hildebrand plot determined the binding affinity for PA and DNP of 1.11×10^5 M^{-1} and 7.41×10^4 M^{-1}, respectively (Fig. 8g and Fig. S26). The results suggested that POSS–Im–An·Br has a greater selectivity for PA than for DNP, aligning with the observed quenching efficiencies. In addition, POSS–Im–An·Br exhibited LOD and LOQ values of 0.72 μM and 2.41 μM for PA, and 0.64 μM and 2.13 μM for DNP, respectively (Table 1 and Fig. S27). The preferential selectivity and affinity towards PA and DNP binding are a result of strong donor–acceptor interactions between the anthracenyl fluorophore and the electron-deficient PA and DNP. The higher number of nitro groups, as electron-withdrawing groups (EWGs), in PA and DNP enhances their sensitivity and selectivity compared to ONP, MNP, PNP, and other NACs (Fig. S28a and S29a).[18,69]

In the case of PAH derivatives, NPY exhibited the most significant quenching (79%), followed by PCA (63%), ACA (49%), NAA (36%), and NNP (22%) (Table 1, Fig. 8b, c and Fig. S24), aligned with the trend of K_{sv} values (Fig. 8e, f and Fig. S25). The binding affinity followed the order: NPY > NAA > ACA > NNP > PCA (Table 1, Fig. 8h, i and Fig. S26). These results suggest that the strength of electron-withdrawing groups (EWGs: NO$_2$ > CHO) significantly affects donor–acceptor interactions, thereby promoting the observed dark emission
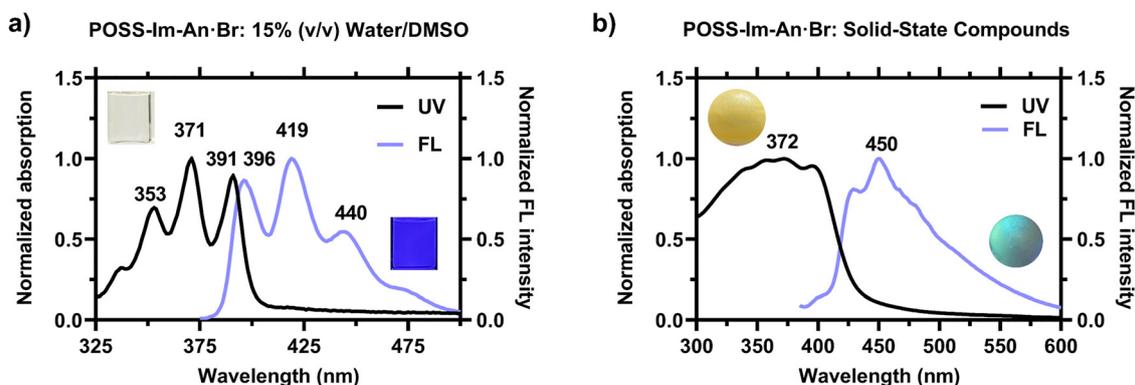

Fig. 5 UV-visible absorption and fluorescence emission spectra of POSS–Im–An·Br in (a) 15% (v/v) water in DMSO solution (1×10^{-6} M) and (b) a solid sample.
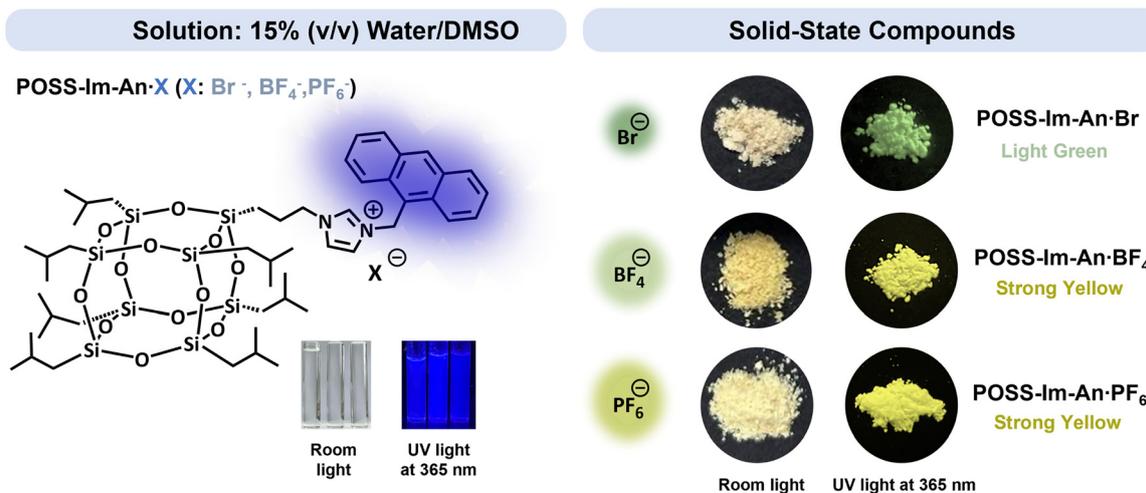
5704 | *J. Mater. Chem. C*, 2026, **14**, 5699–5711

This journal is © The Royal Society of Chemistry 2026

Fig. 6 Fluorescence emission characteristics of POSS−Im−An·Br, POSS−Im−An·BF$_4$, and POSS−Im−An·PF$_6$ as solutions prepared in a mixture of 15% (v/v) water/DMSO and as solid samples under room light and UV light at 365 nm.

Fig. 7 The selected NACs and PAH derivatives employed in this study.

(Fig. S28b and S29b). For PAHs, some derivatives, including PYR, ANT, and BAA, showed fluorescence background signals. The fluorescence enhancement observed upon addition of PAH guests arose from the signal of POSS−Im−An·Br together with PAHs.[36,70] To assess the sensing performance relative to previously reported systems, the K_{sv} values were compared with representative literature data (Table S2). Notably, the K_{sv} value of POSS−Im−An·Br is approximately an order of magnitude higher than those of many reported systems, reflecting its enhanced quenching efficiency and stronger binding capability.

The enhanced sensitivity originates from the cooperative π-donor–π-acceptor interactions between the anthracenyl fluorophore and electron-deficient aromatic analytes, particularly NACs and PAH derivatives bearing –NO$_2$ or –CHO substituents. Consequently, POSS−Im−An·Br is highly promising for field-deployable NAC/PAH detection and integration into portable optical sensing devices.

POSS−Im−An·Br exhibited rapid fluorescence sensing toward PA, DNP, NNP, NAA, ACA, NPY, and PCA (Fig. S30 and Movies S1–S7). The fluorescence intensity dropped rapidly and

This journal is © The Royal Society of Chemistry 2026

J. Mater. Chem. C, 2026, **14**, 5699–5711 | 5705

Table 1 Summary of the determined titration parameters, including quantum efficiency, quenching efficiency, limit of detection (LOD), limit of quantification (LOQ), the Stern–Volmer constants (K_{sv}), and the binding affinity (K_a) of POSS–Im–An·Br in the presence different target analytes

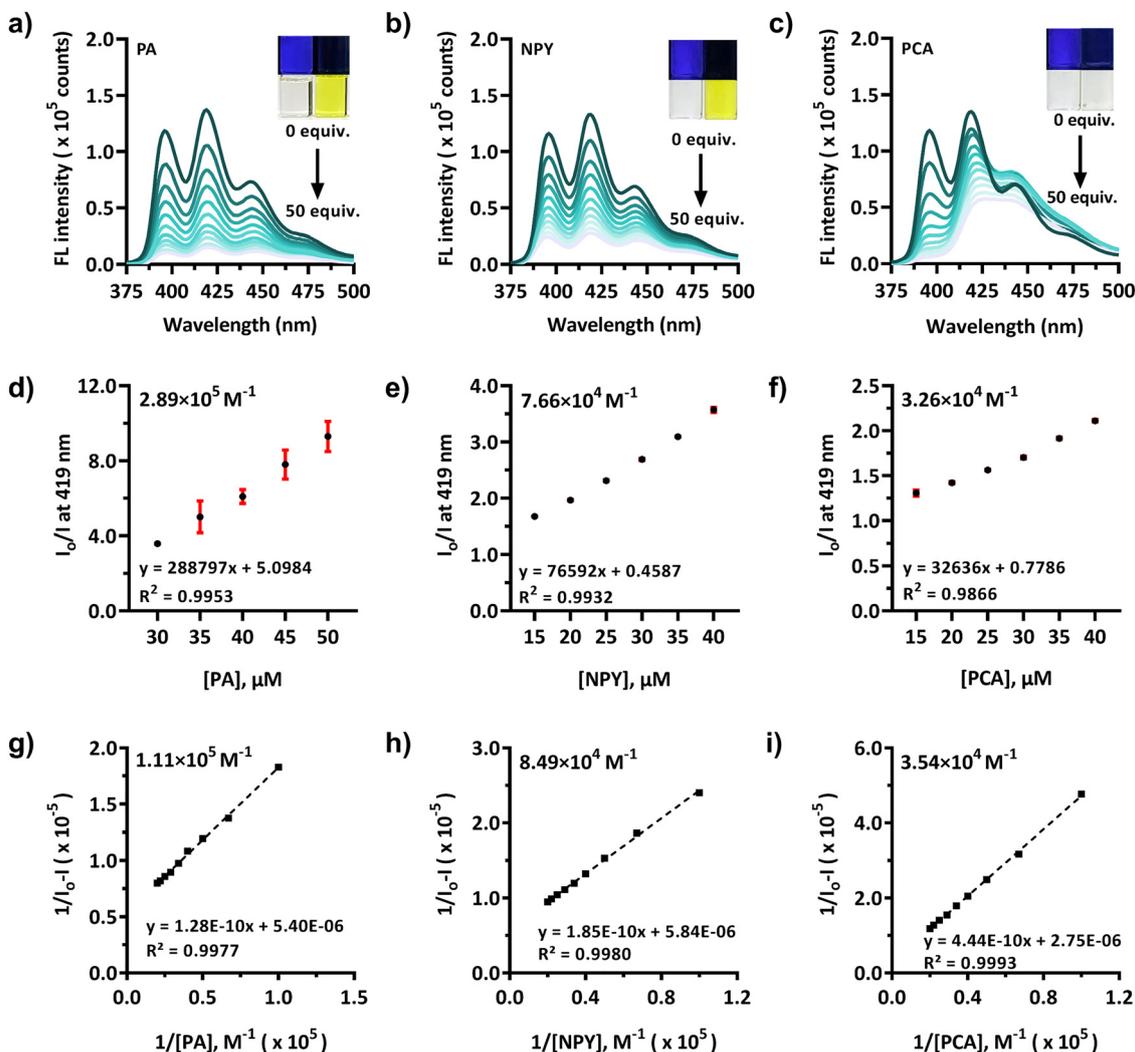| Compounds	Quantum efficiency (%)	Quenching efficiency (%)	LOD (μM)	LOQ (μM)	K_{sv} (M^{-1})	K_a (M^{-1})
POSS–Im–An·Br	15.42	^{a}	^{a}	^{a}	^{a}	^{a}
PA	0.16	89	0.72	2.41	2.89×10^5	1.11×10^5
DNP	0.85	55	0.64	2.13	2.29×10^4	7.41×10^4
ACA	1.86	49	0.84	2.80	1.89×10^4	6.57×10^4
NAA	2.81	36	3.87	12.89	9.80×10^3	7.26×10^4
PCA	0.98	63	0.62	2.06	3.26×10^4	3.54×10^4
NPY	2.98	79	0.54	1.80	7.66×10^4	8.49×10^4
NNP	3.96	22	6.24	20.82	5.04×10^3	6.11×10^4

^{a} Not performed.

Fig. 8 Fluorescence emission spectra of a solution of POSS–Im–An·Br (1×10^{-6} M) in 15% (v/v) water/DMSO in the presence of increasing equivalents of the target analyte from 0 to 50 equiv. of (a) PA, (b) NPY, and (c) PCA. Stern–Volmer plots of POSS–Im–An·Br in the presence of (d) PA, (e) NPY, and (f) PCA. Benesi–Hildebrand plots recorded at λ_{max} = 419 nm obtained from (g) PA, (h) NPY, and (i) PCA.

reached a stable state within a short time. Furthermore, Job's method was used to determine the binding stoichiometry between POSS–Im–An·Br and the analytes. The total concentration of host and guest was kept constant at 1.0×10^{-6} M.[71]

The plots of $\Delta F \times X_h$ versus X_h display maxima at $X_h \approx 0.5$ for all representative analytes (PA, DNP, NNP, NAA, ACA, NPY, and PCA), which is consistent with a predominant 1:1 binding stoichiometry (Fig. S31).[21]

5706 | *J. Mater. Chem. C*, 2026, **14**, 5699–5711

This journal is © The Royal Society of Chemistry 2026

Quantum efficiency

The pristine quantum efficiency of POSS–Im–An·Br in a 15% (v/v) water/DMSO solution was 15.42% but decreased considerably to 0.16% and 0.85% when PA and DNP were added, respectively. The quantum efficiency of electron-deficient PAH derivatives (NNP, NPY, NAA, ACA, and PCA) dropped to 3.96%, 2.98%, 2.81%, 1.86%, and 0.98%, respectively (Table 1 and Fig. S32–S34). The decrease is principally caused by π–donor and π–acceptor interactions between the anthracenyl ring and phenyl groups in NACs and PAH derivatives. These non-covalent interactions promote charge transfer from the fluorophore to the analyte, resulting in non-radiative decay and severe quenching.

The effect of ionic strength

The effect of ionic strength on the sensing behavior of POSS–Im–An·Br towards target analytes was investigated. NaCl solutions with concentrations ranging from 0.00 to 0.60 M were added to adjust high-ionic-strength environments.[72,73] POSS–Im–An·Br demonstrated exceptional tolerance to increasing ionic strength, maintaining strong fluorescence emission across various NaCl concentrations, underlining the potential uses for PA detection under practical conditions. The observed quenching phenomenon can be attributed to non-radiative decay processes involving collisions between the fluorophore and quenching anions (Fig. S35). These interactions result in reduced emission, effectively diminishing the fluorescence intensity of POSS–Im–An·Br in the presence of target analytes.[74]

Effect of anti-interferences and real water sample analysis

NACs and PAH derivatives typically coexist in environmental matrices with abundant inorganic ions that could potentially interfere with fluorescence-based sensing. To evaluate selectivity, the fluorescence response of POSS–Im–An·Br (15% (v/v) H_2O/DMSO) was examined in the presence of 50 equiv. of common additives, including Na^+, K^+, Mg^{2+}, Mn^{2+}, Co^{2+}, Ni^{2+}, Cu^{2+}, Zn^{2+}, Pb^{2+}, Br^-, I^-, NO_3^-, ClO_4^-, HSO_4^-, and SCN^-. These ions produced no measurable interference with the sensing performance toward PA, DNP, NNP, NAA, ACA, NPY, and PCA (Fig. S36–S38).[20–25] Furthermore, POSS–Im–An·Br successfully detected these analytes spiked into real water samples (tap water and mineral water) without a significant matrix effect (Fig. S39 and Table S3), supporting its practical applicability for fluorescence detection in complex aqueous environments.
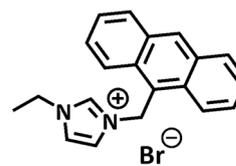
Binding mode studies

^{1}H-NMR titration experiments were performed to gain insight into the binding modes of POSS–Im–An·Br with PA and DNP in d_6-DMSO. Addition of increasing equivalents of PA caused upfield perturbations of proton signals associated with the imidazolium unit (H_b, H_c, and H_d) and the anthracenyl substituent (H_f, H_g, H_h, H_i, and H_j), concomitantly the downfield shift of the aromatic proton signal of PA (H_1). These similar changes were observed in the case of DNP (Fig. S40 and S41).[40,75,76]

Due to the limited solubility in d_6-DMSO, titration experiments with PAH derivatives were carried out in $CDCl_3$. NAA induced the upfield perturbations and broadening of signals associated with H_b, the acidic proton of the imidazolium motif, indicating the dynamic exchange with the surrounding. In addition, other proton signals of the imidazolium unit (H_c and H_d), the anthracenyl substituent (H_f, H_g, H_h, H_i, and H_j), and the NAA guest moved to the upfield region, indicating a strong tendency to engage in π–π interactions with the electron-deficient NAA (Fig. S42).[54,77,78] In the case of ACA, the C–H···O═C hydrogen bonding interactions between H_b and the aldehyde carbonyl resulted in the downfield perturbation of H_b (Fig. S43). In addition, the signals of the POSS moiety are located at 0.56–1.97 ppm and remain unchanged upon the PAH derivative binding. Although POSS did not participate in the binding, it helps preventing the aggregation of the fluorophore as well as restricting the motion. The binding trends observed for other PAH derivatives (NPY, PCA, and NNP) were consistent with those of NAA and ACA (Fig. S44–S46).

DFT computational study

The computational study was conducted using density functional theory (DFT) calculations performed using ORCA 6.0.0 software.[79] The calculations were performed using the aug-cc-pVDZ/ω97x-D3 level of theory in DMSO (SMD model).[80] Consistent with the NMR titration results, the preferred interaction site for both NACs and PAHs was identified at the imidazolium motif. Given the strong experimental indication of imidazolium–analyte interactions, the use of a diffuse-function basis set together with a range-separated functional including dispersion corrections was deemed appropriate to capture noncovalent binding reliably. To reduce computational cost, EtIm-An was selected as a simplified model for POSS–Im–An·Br (Fig. 9). Notably, two local minima were located on the potential energy surface, corresponding to charge–dipole (CD) and π-donor–π–acceptor interactions.

Geometry optimizations show that the CD-binding mode affords more stable complexes than the corresponding π-donor–π-acceptor arrangements for all analytes examined (Fig. 10), highlighting the key role of the imidazolium group in stabilization. This trend agrees with the NMR titration data, particularly for analytes bearing strong electron-withdrawing groups (EWGs) such as –CHO or –NO₂ (e.g., PA, ACA, and NAA). In these complexes, the negatively polarized oxygen atoms engage in favorable electrostatic attraction with the imidazolium fragment. In contrast, the bulky –Br substituent in BAA

Simplified form: EtIm-An

Fig. 9 Simplified form of POSS–Im–An·Br (EtIm–An).

This journal is © The Royal Society of Chemistry 2026

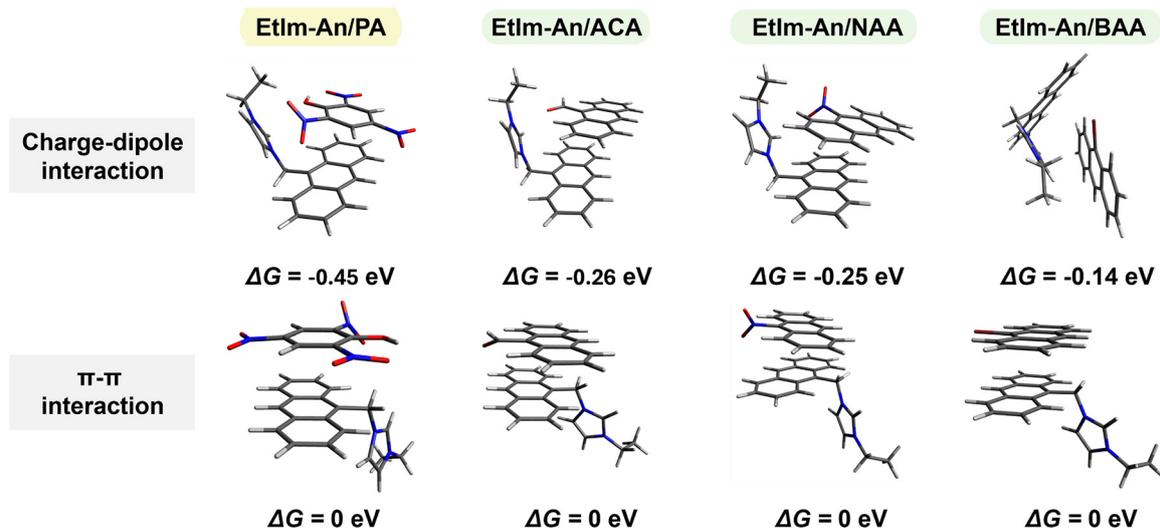*J. Mater. Chem. C*, 2026, **14**, 5699–5711 | 5707

Fig. 10 Geometry optimization of EtIm–An upon interaction with PA, ACA (–CHO), NAA (–NO$_2$), and BAA (–Br) using the aug-cc-pVDZ/ω97x-D3 level of theory in DMSO (SMD model), in 2 local minimum geometries as charge-dipole (CD) interactions and π–π interactions. ΔG is the relative Gibbs free energy of the CD in comparison to π–π interactions of all compounds, which shows that EtIm-An prefers to undergo CD rather than π–π interactions.

suppresses close contact with EtIm-An and thereby disfavors additional π–type interactions (Fig. 10).

Experimentally, electron-deficient NACs and PAH derivatives quench the fluorescence of POSS–Im–An·Br, indicating that photoinduced electron transfer (PET) contributes to the quenching response (Fig. 11).[81–83] PET can be broadly classified into (i) donor-PET (d-PET), where an excited fluorophore donates an electron to the quencher, and (ii) acceptor-PET (a-PET), where the excited fluorophore accepts an electron.[84] Because the analytes studied here are electron-deficient, a d-PET pathway is most reasonable.

In a donor–type PET mechanism, the excited sensor (D*) transfers an electron to the analyte (A), so the analyte's electron-accepting ability, linked to its reduction potential/electron affinity, and thus its LUMO energy is a key determinant of quenching efficiency (Fig. 11). Accordingly, analytes with lower-lying LUMOs (higher electron affinities) are expected to accept an electron more readily and give stronger PET-based responses.

To provide a simple orbital-energy descriptor for this trend, we define $\Delta E_{\text{d-PET}} = \text{LUMO}_{\text{analyte}} - \text{LUMO}_{\text{EtIm-An}}$. More negative $\Delta E_{\text{d-PET}}$ values indicate a more favorable acceptor level relative to the donor model and correlate with easier formation of a low-lying charge-transfer (CT) state. In the absence of quenchers, EtIm-An undergoes excitation from the ground state (S$_0$) to a locally excited (LE) state, followed by emissive relaxation to S$_0$. Upon complexation with a strong electron-accepting analyte (e.g., PA or DNP), a lower-lying CT state becomes accessible; population transfer from LE to CT followed by non-radiative decay leads to fluorescence quenching.

Importantly, the analyte selectivity is dictated by not only $\Delta E_{\text{d-PET}}$ but also sufficient donor–acceptor proximity and electronic coupling, which are controlled by host–guest binding strength and geometry. Thus, orbital/electron-density descriptions
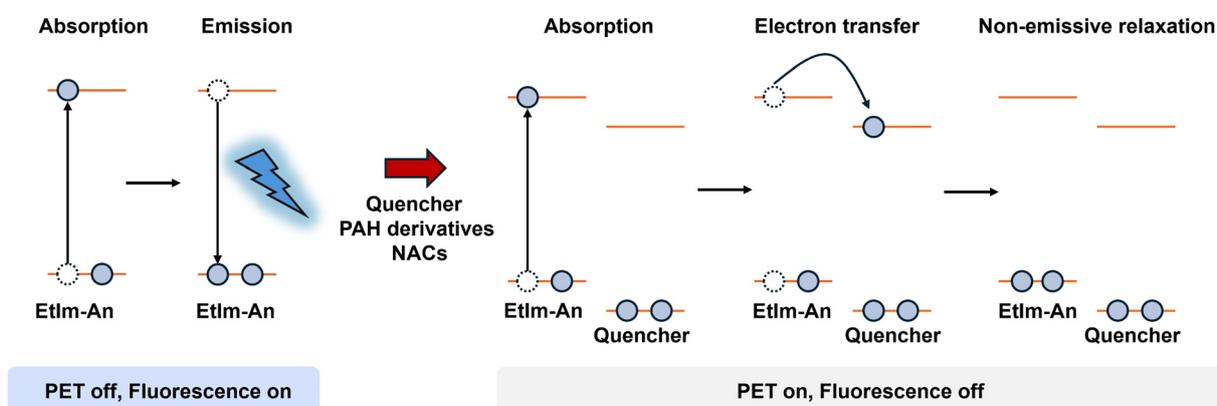

Fig. 11 Proposed quenching mechanism of EtIm-An upon adding analytes, where having a quencher (analyte) causes donor photo-induced electron transfer (d-PET), resulting in non-emissive relaxation.

5708 | *J. Mater. Chem. C*, 2026, **14**, 5699–5711

This journal is © The Royal Society of Chemistry 2026

(e.g., polarization near heteroatoms) are used here to rationalize binding orientation and coupling, rather than PET thermodynamics.

For PAH derivatives, results align with the d-PET scheme. The $\Delta E_{\text{d-PET}}$ values for ACA, NAA, PCA, NPY, and NNP are -0.52, -0.35, -0.25, -0.44, and -0.27 eV, respectively. In contrast, NPA has a $\Delta E_{\text{d-PET}}$ of 0.01 eV, consistent with experimental findings, showing that NPA does not quench fluorescence. This difference reflects the weaker acceptor character (higher-lying LUMO) of NPA compared with more strongly electron-deficient analytes such as PA and DNP, where multiple $-NO_2$ groups substantially lower the LUMO and stabilize the CT state (Fig. S47a and b).[85]

For NACs, EtIm-An shows pronounced selectivity toward compounds bearing multiple $-NO_2$ groups. PA and DNP exhibit strongly negative $\Delta E_{\text{d-PET}}$ values (-1.63 and -1.08 eV, respectively) and the most efficient quenching. By comparison, MNP, PNB, and ONP show less negative values, while the remaining analytes display positive $\Delta E_{\text{d-PET}}$ (Fig. S47c and d), indicating a reduced thermodynamic tendency for electron transfer. In addition, geometry optimizations reveal that in the PA complex the $-NO_2$ groups orient toward the imidazolium ring, enhancing charge polarization and electrostatic stabilization. Although PNB has a $\Delta E_{\text{d-PET}}$ comparable to DNP, its single $-NO_2$ group provides weaker oxygen polarization and less effective interfacial electrostatic stabilization, diminishing CT-state stabilization and thereby reducing the overall quenching response.

Conclusions

In this work, we have successfully designed, synthesized, and characterized a series of imidazolium-functionalized polyhedral oligomeric silsesquioxanes incorporating anthracene (POSS–Im–An·X, X = Br, BF$_4$, PF$_6$) as an electron-rich fluorophore for the preferential fluorescence detection of NACs and PAH derivatives. The synergistic combination of the POSS core, imidazolium spacer, and anthracene moiety endows the sensor with enhanced aqueous compatibility, thermal stability, and strong fluorescence emission in mixed aqueous–organic solutions. Photophysical studies revealed that POSS–Im–An·Br exhibited a pronounced and analyte-dependent fluorescence response toward PA, DNP, and electron-deficient PAH derivatives, with the LOD in the micromolar range. Mechanistic investigations through ^{1}H-NMR titrations, computational modelling, and Stern–Volmer analysis indicate that charge–dipole interactions and π–π interactions control the binding mode that results in the quenching of fluorescence signals via the d-PET pathway. The nature of counter anions significantly influences solid-state emission properties through ion-pairing and packing effects. Additionally, the sensor demonstrates robust performance under varying ionic strengths, underscoring its potential for real-world environmental monitoring. Overall, POSS–Im–An·Br exhibits an analyte-dependent and preferential fluorescence response toward selected NACs and PAH

derivatives, while maintaining sensing performance under competitive and interfering conditions, highlighting its potential for fluorescence detection in complex aqueous environments. These findings open avenues for the development of advanced POSS-based sensing materials for environmental safety, pollutant remediation, and on-site chemical analysis.

Author contributions

The manuscript was written through the contributions of all authors. All authors have approved the final version of the manuscript.

Conflicts of interest

The authors declare no competing financial interest.

Data availability

The data supporting this article have been included as part of the supplementary information (SI). Supplementary information: characterization of compounds, titration data, and computational data (file type, i.e., PDF). See DOI: https://doi.org/10.1039/d5tc03926f.

Acknowledgements

References

1 P. Romundstad, T. Haldorsen and A. Rønneberg, Am. J. Ind. Med., 1999, 35, 164–174.

2 K.-S. Ju and E. Parales Rebecca, Microbiol. Mol. Biol. Rev., 2010, 74, 250–272.

3 M. S. Macias, PhD thesis, Florida International University, 2009.

4 S. Madhu, A. Bandela and M. Ravikanth, RSC Adv., 2014, 4, 7120–7123.

5 I. A. Popov, H. Chen, O. N. Kharybin, E. N. Nikolaev and R. G. Cooks, Chem. Commun., 2005, 1953–1955.

This journal is © The Royal Society of Chemistry 2026

J. Mater. Chem. C, 2026, 14, 5699–5711 | 5709

6 S. A. Nsibande, H. Montaseri and P. B. C. Forbes, *TrAC, Trends Anal. Chem.*, 2019, **115**, 52–69.

7 B. Todee, T. Chutimasakul, K. Junthod, A. Docker, P. Saetear, M. Kongkaew, T. Ratvijitvech, J. Tantirungrotechai and T. Bunchuay, *Mater. Chem. Front.*, 2022, **6**, 3023–3032.

8 R. Hodyss and J. L. Beauchamp, *Anal. Chem.*, 2005, **77**, 3607–3610.

9 S. Singh, *J. Hazard. Mater.*, 2007, **144**, 15–28.

10 T. H. Noh, H. Lee, J. Jang and O.-S. Jung, *Angew. Chem., Int. Ed.*, 2015, **54**, 9284–9288.

11 J. M. Sylvia, J. A. Janni, J. D. Klein and K. M. Spencer, *Anal. Chem.*, 2000, **72**, 5834–5840.

12 G. A. Eiceman and J. A. Stone, *Anal. Chem.*, 2004, **76**, 390a–397a.

13 T. Griffin, N. Popkie, M. Eagan, R. McAtee, D. Vrazel and J. McKinly, *Instrument response measurements of ion mobility spectrometers in situ: maintaining optimal system performance of fielded systems*, SPIE, 2005.

14 X. Shen, Y. Cui, Y. Pang and H. Qian, *Electrochim. Acta*, 2012, **59**, 91–99.

15 T. M. Gutiérrez-Valencia and M. P. García de Llasera, *Food Chem.*, 2017, **223**, 82–88.

16 T. Portoles, B. Garlito, J. Nácher-Mestre, M. H. Berntssen and J. Pérez-Sánchez, *Talanta*, 2017, **172**, 109–119.

17 H. Sohn, R. M. Calhoun, M. J. Sailor and W. C. Trogler, *Angew. Chem., Int. Ed.*, 2001, **40**, 2104–2105.

18 X. Tian, X. Qi, X. Liu and Q. Zhang, *Sens. Actuators, B*, 2016, **229**, 520–527.

19 Z. Ma, T. Wu, P. Li, M. Liu, S. Huang, H. Li, Y. Zhang and S. Yao, *Microchim. Acta*, 2019, **186**, 498.

20 B.-W. Wang, K. Jiang, J.-X. Li, S.-H. Luo, Z.-Y. Wang and H.-F. Jiang, *Angew. Chem., Int. Ed.*, 2020, **59**, 2338–2343.

21 X. Zhuang, N. Zhang, X. Zhang, Y. Wang, L. Zhao and Q. Yang, *Microchem. J.*, 2020, **153**, 104498.

22 M. Ashafaq, M. Khalid, M. Raizada, M. S. Ahmad, M. S. Khan, M. Shahid and M. Ahmad, *J. Inorg. Organomet. Polym. Mater.*, 2020, **30**, 4496–4509.

23 M. Li, J. Ma, J. Wang, X. Wei and W. Lu, *ACS Appl. Mater. Interfaces*, 2025, **17**, 4033–4043.

24 S. B. Lee, J. Heo, S. Noh, T. E. An, G. Kim, G. M. Lee, J. Kim, K. Kim, J. Lee, T. Kim, C. Song and H. Y. Bae, *Adv. Sci.*, 2025, **12**, e06616.

25 Z.-H. Chen, Z.-J. Chen, Y. Zeng, Y.-T. Liang, J.-L. Guo, S.-H. Yang and Z.-Y. Wang, *Spectrochim. Acta, Part A*, 2025, **326**, 125281.

26 K. Junthod, P. Srisawat, P. Laoviwat, N. Watanabe, P. Tangsasom, A. Srevattanangkul, P. Kaeopookum, T. Sangtawesin, B. Todee, Y. Shigeta, K. Hengphasartporn, J. Tantirungrotechai and T. Bunchuay, *Sep. Purif. Technol.*, 2026, **382**, 135782.

27 S. Shaligram, P. P. Wadgaonkar and U. K. Kharul, *J. Mater. Chem. A*, 2014, **2**, 13983–13989.

28 N. Niamnont, N. Kimpitak, K. Wongravee, P. Rashatasakhon, K. K. Baldridge, J. S. Siegel and M. Sukwattanasinitt, *Chem. Commun.*, 2013, **49**, 780–782.

29 B. Gole, W. Song, M. Lackinger and P. S. Mukherjee, *Chem. – Eur. J.*, 2014, **20**, 13662–13680.

30 M. E. Germain and M. J. Knapp, *J. Am. Chem. Soc.*, 2008, **130**, 5422–5423.

31 G. He, H. Peng, T. Liu, M. Yang, Y. Zhang and Y. Fang, *J. Mater. Chem.*, 2009, **19**, 7347–7353.

32 S. W. Thomas, G. D. Joly and T. M. Swager, *Chem. Rev.*, 2007, **107**, 1339–1386.

33 J. S. Park, F. Le Derf, C. M. Bejger, V. M. Lynch, J. L. Sessler, K. A. Nielsen, C. Johnsen and J. O. Jeppesen, *Chem. – Eur. J.*, 2010, **16**, 848–854.

34 Z. Li, Y. Zhang, T. Cao, Y. Yang, Y. Xiong, S. Xu and Z. Xu, *J. Membr. Sci.*, 2017, **541**, 474–482.

35 F. Zou, H. Ling, L. Zhou, F. Wang and Y. Li, *Dyes Pigm.*, 2021, **184**, 108840.

36 S. A. Wahurwagh, S. Bhagat, A. S. Talmale, A. V. Wankhade, S. P. Zodape and U. R. Pratap, *J. Inorg. Organomet. Polym. Mater.*, 2025, **35**, 4285–4299.

37 H. Chabane, S. Livi, H. Benes, C. Ladavière, P. Ecorchard, J. Duchet-Rumeau and J.-F. Gérard, *Eur. Polym. J.*, 2019, **114**, 332–337.

38 T. Bureerug, C. Wannasiri, S. Chanmungkalakul, M. Sukwattanasinitt, V. Ervithayasuporn and T. Bunchuay, *Polym. Chem.*, 2024, **15**, 2981–2991.

39 R. Sodkhomkhum, M. Masik, S. Watchasit, C. Suksai, J. Boonmak, S. Youngme, N. Wanichacheva and V. Ervithayasuporn, *Sens. Actuators, B*, 2017, **245**, 665–673.

40 C. Pherkkhuntod, V. Ervithayasuporn, S. Chanmungkalakul, C. Wang, X. Liu, D. J. Harding and S. Kiatkamjornwong, *Sens. Actuators, B*, 2021, **330**, 129287.

41 C.-H. Lu, C.-H. Tsai, F.-C. Chang, K.-U. Jeong and S.-W. Kuo, *J. Colloid Interface Sci.*, 2011, **358**, 93–101.

42 P. Siripanich, T. Bureerug, S. Chanmungkalakul, M. Sukwattanasinitt and V. Ervithayasuporn, *Organometallics*, 2022, **41**, 201–210.

43 D. Ning, Q. Liu, Q. Wang, X.-M. Du, Y. Li and W.-J. Ruan, *Dalton Trans.*, 2019, **48**, 5705–5712.

44 T. Khianjinda, S. Vigromsitdet, P. Srisawat, N. Sawektreeratana, J. Tantirungrotechai, M. Sukwattanasinitt, D. J. Harding, P. D. Beer, Y. Tantirungrotechai and T. Bunchuay, *Inorg. Chem.*, 2026, **65**, 441–453.

45 Y. El Aziz, N. Mehrban, P. G. Taylor, M. A. Birchall, J. Bowen, A. R. Bassindale, M. B. Pitak and S. J. Coles, *RSC Adv.*, 2017, **7**, 37474–37477.

46 Y. Li, X.-H. Dong, Y. Zou, Z. Wang, K. Yue, M. Huang, H. Liu, X. Feng, Z. Lin, W. Zhang, W.-B. Zhang and S. Z. D. Cheng, *Polymer*, 2017, **125**, 303–329.

47 C. Azap, D. Wolf, D. Abbenhuis, H. C. L. Gerritsen, G. Grela, K. Wilting, J. B. M. Leszczynska, K. Czaban, J. Wojtasiewicz and A. Germany, *Eur. Pat.*, EP2368894, 2011.

48 V. Ervithayasuporn, X. Wang and Y. Kawakami, *Chem. Commun.*, 2009, 5130–5132.

49 A. Fina, D. Tabuani, F. Carniato, A. Frache, E. Boccaleri and G. Camino, *Thermochim. Acta*, 2006, **440**, 36–42.

50 A. I. Bram, I. Gouzman, A. Bolker, N. Eliaz and R. Verker, *Molecules*, 2020, **25**, 4203.

51 F. Constantin, S. A. Gârea and H. Iovu, *Composites, Part B*, 2013, **44**, 558–564.

5710 | *J. Mater. Chem. C*, 2026, **14**, 5699–5711

This journal is © The Royal Society of Chemistry 2026

52 V. Lakshmidevi, P. Parvathi and A. Venkataraman, *MJAI*, 2017, **2**(1), 21–24.

53 D. Affandi, S. J. Berners-Price, P. J. Harvey, P. C. Healy, B. E. Ruch and A. H. White, *J. Chem. Soc., Dalton Trans.*, 1997, 1411–1420.

54 G. Jha, P. K. Sahu, S. Panda, D. V. Singh, S. Patole, H. Mohapatra and M. Sarkar, *ChemistrySelect*, 2017, **2**, 2426–2432.

55 Z. Kausar, A. Mansha and S. Asim, *J. Fluoresc.*, 2024, **34**, 1365–1378.

56 H. Xie, H. Wang, Z. Xu, R. Qiao, X. Wang, X. Wang, L. Wu, H. Lu and S. Feng, *J. Mater. Chem. C*, 2014, **2**, 9425–9430.

57 Z. Chen, D. Wang, S. Feng and H. Liu, *ACS Appl. Mater. Interfaces*, 2021, **13**, 23592–23605.

58 H. Wu, M. Li, C. Sun, X. Wang and Z. Su, *Dalton Trans.*, 2020, **49**, 5087–5091.

59 J. Mei, N. L. C. Leung, R. T. K. Kwok, J. W. Y. Lam and B. Z. Tang, *Chem. Rev.*, 2015, **115**, 11718–11940.

60 Q. Feng, M. Wang, B. Dong, C. Xu, J. Zhao and H. Zhang, *CrystEngComm*, 2013, **15**, 3623–3629.

61 J. N. Gayton, S. Autry, R. C. Fortenberry, N. I. Hammer and J. H. Delcamp, *Molecules*, 2018, **23**, 3051.

62 Y. Hu, S. Long, H. Fu, Y. She, Z. Xu and J. Yoon, *Chem. Soc. Rev.*, 2021, **50**, 589–618.

63 K. Nobuoka, S. Enoki, H. Tanaka and S. Kitaoka, *J. Ion. Liq.*, 2025, **5**, 100137.

64 J.-H. Wei, Y. Xiao, J.-B. Luo, Z.-L. He, J.-H. Chen, Q.-P. Peng and D.-B. Kuang, *Chem. Sci.*, 2025, **16**, 7239–7248.

65 S. Pandey, *Anal. Chim. Acta*, 2006, **556**, 38–45.

66 T. Zhou, L. Chen, Y. Ye, L. Chen, Z. Qi, H. Freund and K. Sundmacher, *Ind. Eng. Chem. Res.*, 2012, **51**, 6256–6264.

67 H. Östmark, S. Wallin and H. G. Ang, *Propellants, Explos., Pyrotech.*, 2012, **37**, 12–23.

68 P. Thordarson, *Chem. Soc. Rev.*, 2011, **40**, 1305–1323.

69 B. Roy, A. K. Bar, B. Gole and P. S. Mukherjee, *J. Org. Chem.*, 2013, **78**, 1306–1310.

70 N. S. Alsadun, A. A. Alfadil, A. A. Elbashir, F. O. Suliman, M. M. Ali Omar and A. Y. Ahmed, *Molecules.*, 2024, **29**, 2535.

71 D. Vinayagam and K. Subramanian, *RSC Adv.*, 2024, **14**, 5149–5158.

72 H. Yang, G. Ran, J. Yan, H. Zhang and X. Hu, *Luminescence*, 2018, **33**, 349–355.

73 K. V. Joshi, B. K. Joshi, A. Pandya, P. G. Sutariya and S. K. Menon, *Analyst*, 2012, **137**, 4647–4650.

74 R. W. Stoughton and G. K. Rollefson, *J. Am. Chem. Soc.*, 1939, **61**, 2634–2638.

75 P. Vishnoi, S. Sen, G. N. Patwari and R. Murugavel, *New J. Chem.*, 2015, **39**, 886–892.

76 Q. Liu, S. Yu, Z. Zhao, X. Zhang and R. Liu, *Dyes Pigm.*, 2020, **173**, 107983.

77 A. Garci, Y. Beldjoudi, M. S. Kodaimati, J. E. Hornick, M. T. Nguyen, M. M. Cetin, C. L. Stern, I. Roy, E. A. Weiss and J. F. Stoddart, *J. Am. Chem. Soc.*, 2020, **142**, 7956–7967.

78 A. P. Singh and J. B. Baruah, *ACS Omega*, 2023, **8**, 30776–30787.

79 F. Neese, *Wiley Interdiscip. Rev.: Comput. Mol. Sci.*, 2012, **2**, 73–78.

80 A. V. Marenich, C. J. Cramer and D. G. Truhlar, *J. Phys. Chem. B*, 2009, **113**, 6378–6396.

81 Y. Feng, J. Liu, M. Lv, P. Xie, H. He and S. Yin, *J. Photochem. Photobiol., A*, 2023, **445**, 115035.

82 J. Harathi, R. Selva Kumar, S. K. Ashok Kumar, D. Saravanakumar, S. Senthilkumar and K. Thenmozhi, *J. Mater. Chem. C*, 2022, **10**, 7949–7961.

83 E. V. Verbitskiy, Y. A. Kvashnin, A. A. Baranova, K. O. Khokhlov, R. D. Chuvashov, I. Y. E. Schapov, Y. A. Yakovleva, E. F. Zhilina, A. V. Shchepochkin, N. I. Makarova, E. V. Vetrova, A. V. Metelitsa, G. L. Rusinov, O. N. Chupakhin and V. N. Charushin, *Dyes Pigm.*, 2020, **178**, 108344.

84 W. Chi, J. Chen, W. Liu, C. Wang, Q. Qi, Q. Qiao, T. M. Tan, K. Xiong, X. Liu, K. Kang, Y.-T. Chang, Z. Xu and X. Liu, *J. Am. Chem. Soc.*, 2020, **142**, 6777–6785.

85 Y. Mao, M. Head-Gordon and Y. Shao, *Chem. Sci.*, 2018, **9**, 8598–8607.

This journal is © The Royal Society of Chemistry 2026

J. Mater. Chem. C, 2026, **14**, 5699–5711 | **5711**